

# Nanofluidic Transport Theory with Enhancement Factors Approaching One

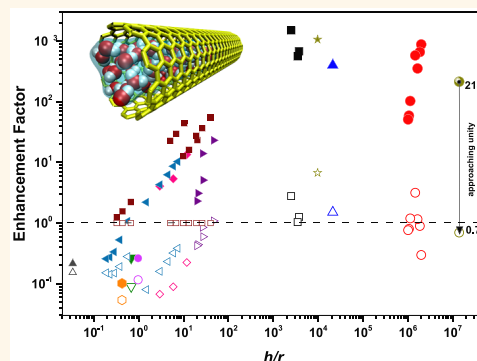
Mohammad Heiranian<sup>1b</sup> and Narayana R. Aluru<sup>\*</sup>

Department of Mechanical Science and Engineering, Beckman Institute for Advanced Science and Technology, University of Illinois at Urbana–Champaign, Urbana, Illinois 61801, United States

## S Supporting Information

**ABSTRACT:** High performance water transport in nanopores has drawn a great deal of attention in a variety of applications, such as water desalination, power generation, and biosensing. High water transport enhancement factors in carbon-based nanopores have been reported over the classical Hagen–Poiseuille (HP) equation which does not account for the physics of transport at molecular scale. Instead, comparing the experimentally measured transport rates to that of a theory, that accounts for the microscopic physics of transport, would result in enhancement factors approaching unity. Such a theory is currently missing. Here, molecular corrections are introduced into the HP equation by considering the variation of key hydrodynamical properties (viscosity and friction) with thickness and diameter of pores in ultrathin graphene and finite-length carbon nanotubes (CNTs) using Green–Kubo relations and molecular dynamics (MD) simulations. The corrected HP (CHP) theory successfully predicts the permeation rates from nonequilibrium MD pressure driven flows. The previously reported enhancement factors over no-slip HP (of the order of 1000) approach unity when the permeations are normalized by the CHP flow rates. The results of our study will help better understand nanoscale flows in carbon-based pores and tubes.

**KEYWORDS:** graphene nanopores, carbon nanotubes, hydrodynamics, thickness-dependent transport, slip length, viscosity, molecular dynamics



Recent advances in nanotechnology and nanofabrication<sup>1,2</sup> combined with unique properties<sup>3–9</sup> of water transport in nanopores and nanotubes have led to significant advances in, for example, membrane technology. Due to the high flux and enhanced selectivity properties, nanoporous membranes have been found to be excellent candidates for water desalination,<sup>10,11</sup> electric power generation,<sup>12</sup> and biological sensing applications.<sup>1,13–15</sup> Water transport rates in carbon-based nanopores have been shown to be several orders of magnitude larger than the rates predicted by the classical no-slip Hagen–Poiseuille (HP) equation.<sup>5–7,16</sup> In carbon nanotubes (CNTs), enhanced flow rates are attributed to the highly frictionless and smooth surfaces.<sup>7,8,17</sup> Ultrathin nanoporous membranes (e.g., single-layer graphene) exhibit high transport rates<sup>11,18–22</sup> as, classically, water flux scales inversely with the membrane thickness.<sup>23</sup> The exceptionally high fluxes obtained with carbon-based membranes have led to the definition of enhancement factors (EFs),<sup>6,24,25</sup> where the experimentally measured or computationally determined (using, for example, molecular dynamics (MD) simulations) flow rates are normalized by the flow rates computed using the classical theory (typically the HP theory), expressed as  $EF = \frac{Q_{EXP/NEMD}}{Q_{HP}}$ .

While the enhancement factors are exciting and indicate the

significance of carbon-based and other materials for nanofluidic transport, an important question arises as to whether the classical theory, which does not account for molecular physics that plays an important role at interfaces and under confinement, can be used to define EFs. Indeed, if a theory that accounts for all the microscopic physics is used to compute the flow rates, one would expect EFs to approach unity. However, such a theory is currently missing, and in this work we report on important molecular physics that can be incorporated into the classical HP theory which can lead to EFs approaching unity ( $EF \rightarrow 1$ ), i.e.,  $EF = \frac{Q_{EXP/NEMD}}{Q_{CHP}} \rightarrow 1$ .

To develop the corrected HP (CHP) theory, we characterize the thickness and diameter dependent flow by considering ultrathin graphene and finite-length CNTs. The variation of hydrodynamic properties such as interfacial friction, slip, and viscosity is studied for various thickness and diameter pores. By accounting for the variation of the key hydrodynamical properties, we develop a corrected HP equation with size dependent relations. Flow rates for pressure driven flows

Received: June 3, 2019

Accepted: December 19, 2019

Published: December 19, 2019

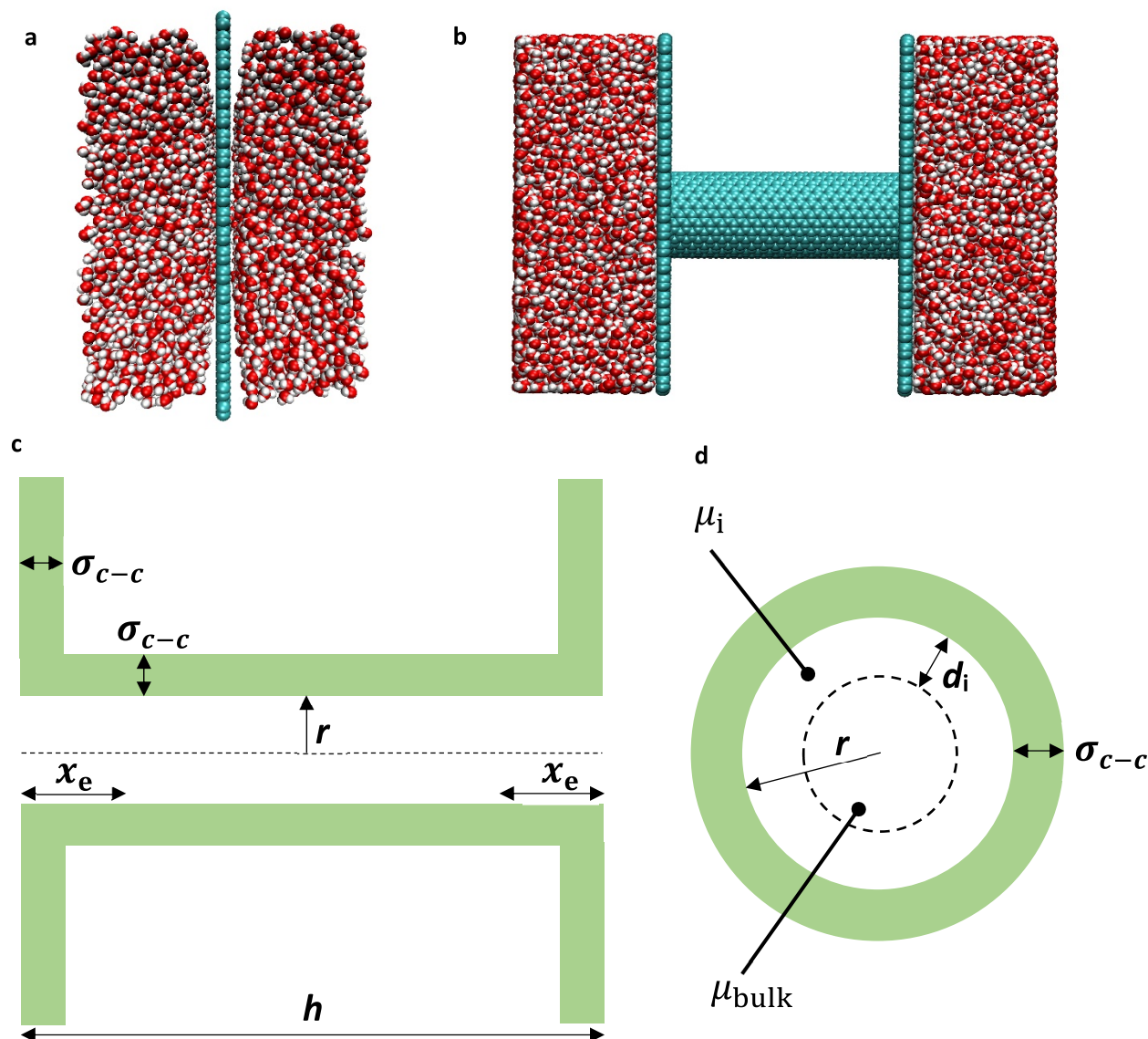


**Figure 1.** a) Simulation box for water across a monolayer graphene nanopore. b) Simulation box for water across a 5 nm-long (14,14) CNT with a graphene sheet at both ends of the tube. c)  $h$ ,  $x_e$ ,  $\sigma_{c-c}$ , and  $r$  are shown for a CNT. The CNT and graphene walls are shown in green. The dashed line represents the centerline of the pore.  $h$  is the physical thickness of each pore including the size of the carbon atom ( $\sigma_{c-c}$ ).  $r$  is the water accessible radius of the pore.  $l$  denotes the combined length of both end regions which is given by  $l = 2x_e(1 - e^{-h/2x_e})$  where  $l$  approaches  $2x_e$  for large  $h$  ( $h > 2x_e$ ), and  $l$  approaches  $h$  for small  $h$  ( $h < 2x_e$ ). d) Cross-sectional view of a CNT where the interfacial annular region, bulk-like region,  $r$ ,  $d_i$ , and  $\sigma_{c-c}$  are shown.  $d_i$  is the thickness of the interfacial annular region.

obtained from nonequilibrium molecular dynamics (NEMD) and published experimental data indicate that the corrected HP equation can provide EFs approaching unity. In a few cases, EFs deviating from unity are observed, and possible reasons for this are discussed.

## RESULTS AND DISCUSSION

**Scaling of Interfacial Friction, Viscosity, and Slip Length.** A typical simulation box consists of water molecules, two graphene sheets (the end walls), and a CNT in between the sheets. In the case of a graphene nanopore system, there are only a single graphene sheet and water molecules. A nanopore (close to the diameter of a CNT) is drilled in each graphene sheet. (6,6), (8,8), (10,10), (14,14), (18,18), and (26,26) CNTs (the corresponding center-to-center diameters are 0.81 nm, 1.08 nm, 1.36 nm, 1.90 nm, 2.44 nm, and 3.53 nm, respectively) with

center-to-center thicknesses (the distance between the centers of the carbon atoms at the two ends of the tubes) of 5 nm, 10 nm, and 20 nm are considered in this study. The system dimensions vary from 3.75 to 11.25 nm in  $x$  and  $y$  and 6 to 26 nm in  $z$  (which is along the axis of the pores) depending on the diameter and thickness of the pores. The dimensions in  $x$  and  $y$  change with the diameter to account for the porosity of the nanopores. The simulations contain about 16,000–110,000 atoms. A typical schematic of the simulation box for a graphene nanopore and CNT is shown in Figure 1. In equilibrium MD (EMD) simulations, friction coefficient ( $\lambda$ ) and viscosity ( $\mu$ ) are obtained using the Green–Kubo formalisms<sup>26,27</sup>

$$\lambda = \frac{1}{K_B T A} \int_0^\infty \langle F(0) \cdot F(t) \rangle dt$$

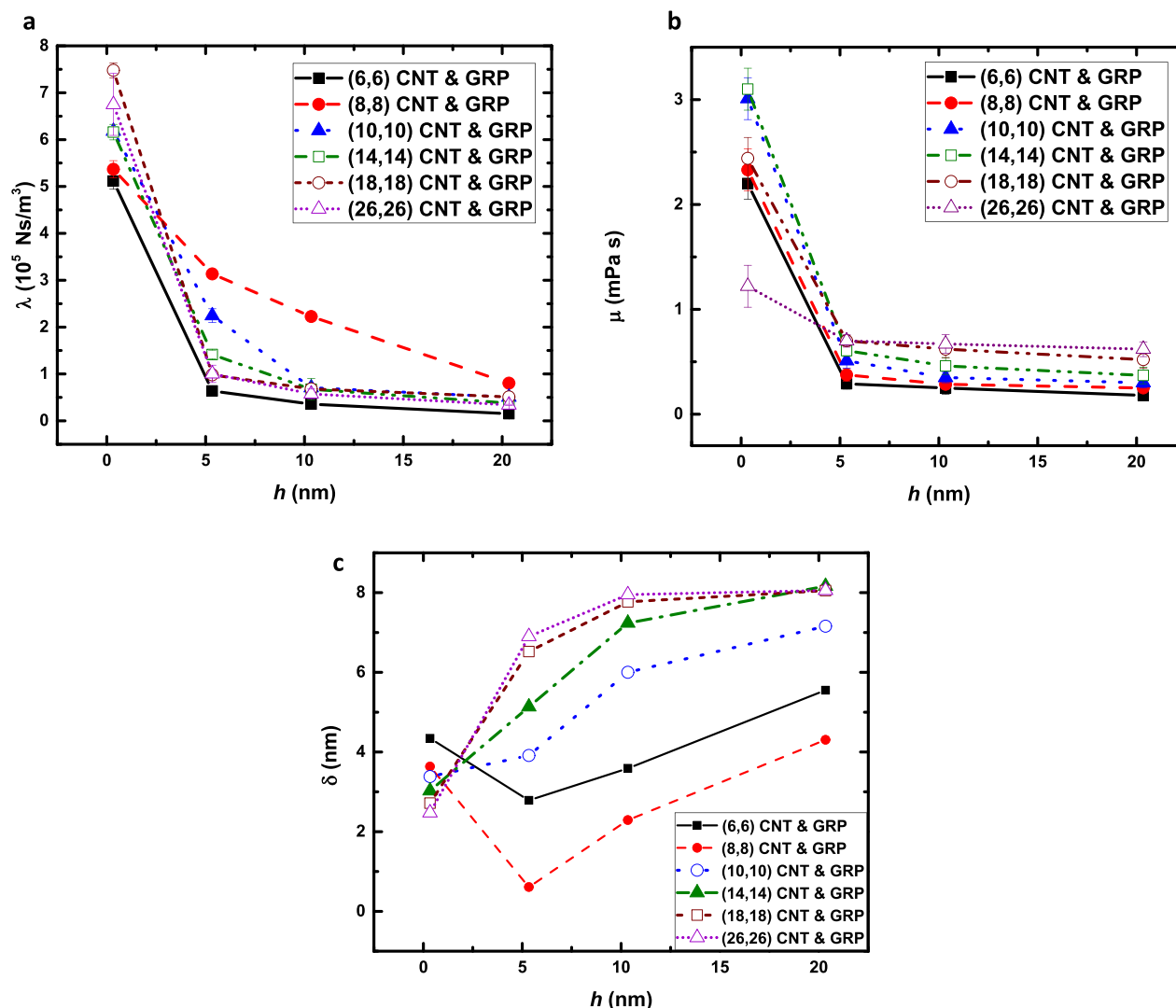


**Figure 2.** Interfacial friction coefficient (a), viscosity (b), and slip length (c) inside the nanopores are plotted as a function of the physical thickness of the nanopores ( $h$ ) for different diameters. The graphene nanopores (denoted as GRP with  $h = 0.34$  nm) and CNTs have similar diameters.  $\lambda$  and  $\mu$  decrease with an increase in thickness. Friction is high at the ends increasing the overall friction in short nanopores. Viscosity is higher in short nanopores due to density layering at the ends. Slip length changes with thickness following the scaling of  $\frac{\mu}{\lambda}$ . As thickness increases, the values of friction, viscosity, and slip length approach that of infinitely long CNTs.

and

$$\mu_{ab} = \frac{V}{K_B T} \int_0^\infty \langle P_{ab}(0) \cdot P_{ab}(t) \rangle dt$$

respectively.  $K_B$ ,  $T$ ,  $A$ ,  $V$ ,  $F(t)$ , and  $P_{ab}(t)$  are the Boltzmann constant, temperature, nanopore surface area, nanopore volume, total wall–fluid axial force, and stress tensor, respectively. Note that  $A$  and  $V$  are calculated based on the water accessible diameter of pores (carbon–carbon Lennard-Jones (LJ) parameter,  $\sigma_{c-c}$  subtracted from carbon center-to-center diameter).  $ab$  are the  $xz$  and  $yz$  components of the stress tensor,  $P_{ab} = \frac{1}{V} \left( \sum_i^N \frac{p_{ia} p_{ib}}{m_i} + \frac{1}{2} \sum_i^N \sum_{j \neq i}^N r_{ija} F_{ijb} \right)$  where  $i$  and  $j$  are atom indices,  $N$  is the number of atoms,  $p_i$  is the momentum of atom  $i$ ,  $m_i$  is the mass of atom  $i$ , and  $r_{ij}$  and  $F_{ij}$  are the distance and force between the pair of atoms  $i$  and  $j$ , respectively. Since the flow is in the  $z$ -direction (the axis of the tube), we are only interested in the  $xz$  and  $yz$  components of the stress tensor for the viscosity calculation. Therefore, we consider the mean of the  $xz$  and  $yz$

components of viscosity in the CNT as the shear viscosity along the flow direction.  $\lambda$  and  $\mu$  are calculated within the physical thickness of each pore/tube ( $h$ ) including the size of carbon atoms at the ends. In this work, “end region” refers to the region inside the pore/tube as shown in Figure 1c. In graphene nanopores, the carbon–carbon LJ parameter,  $\sigma_{c-c} = 0.34$  nm, is taken as the physical thickness ( $h$ ) of the membrane. As shown in Figure 1c, in CNTs,  $h$  is the addition of the center-to-center thickness and  $\sigma_{c-c}$  (e.g., for the CNT with the center-to-center thickness of 5 nm, the physical thickness is given by  $h = 5$  nm +  $\sigma_{c-c} = 5.34$  nm). As shown in Figure 1d, for the variation of viscosity with diameter, a two-viscosity model (as discussed later in the manuscript) is considered with a core viscosity modeled as the bulk viscosity and an interfacial viscosity denoted by  $\mu_i$  with a layer thickness of  $d_i$ . The cumulative integrals of the Green–Kubo auto correlation functions as a function of time are provided for one nanopore size in the Supporting Information (Figure S1).

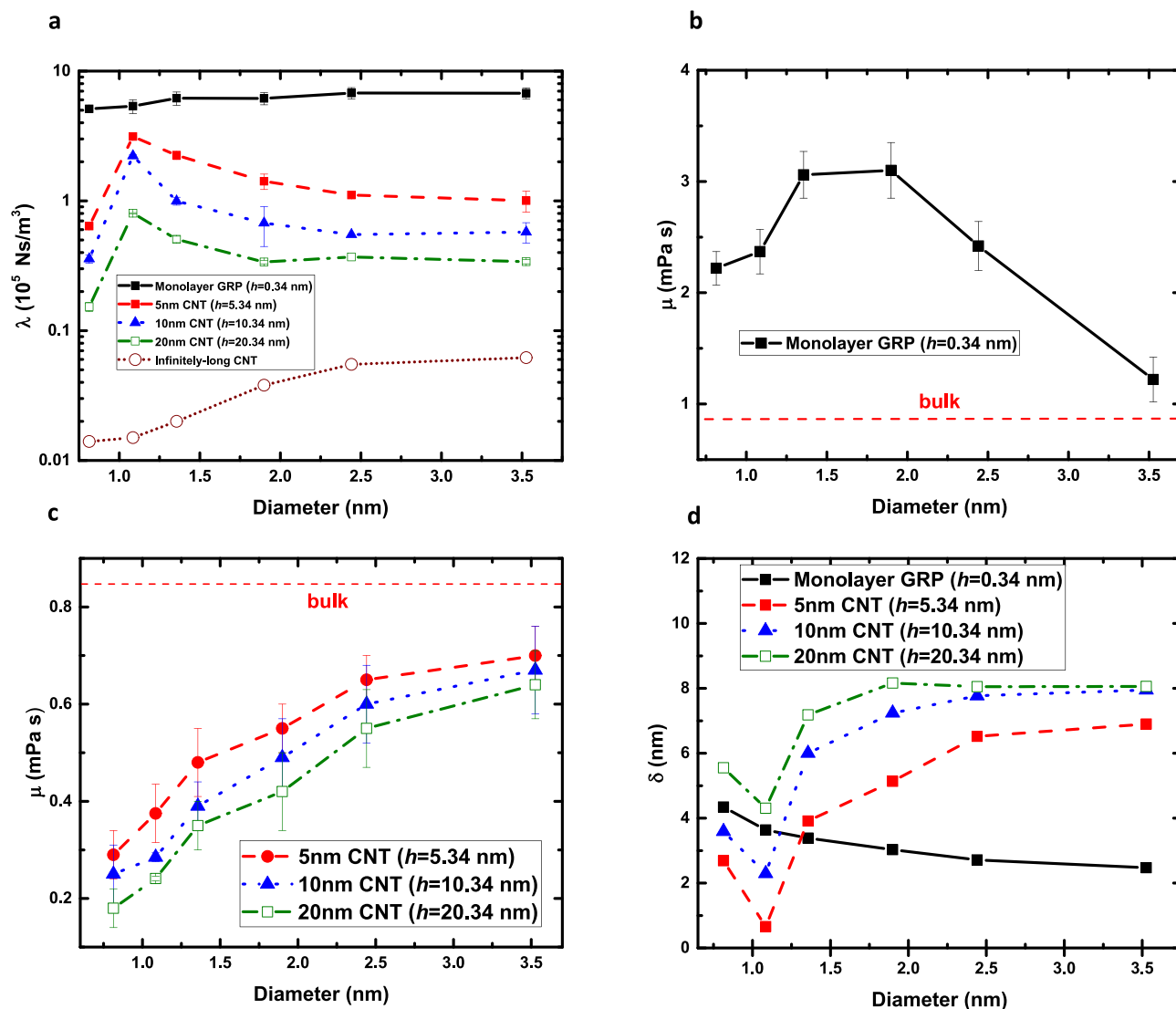


**Figure 3.** Interfacial friction coefficient (a), viscosity in monolayer graphene (b), viscosity in finite-length CNTs (c), and slip length (d) are plotted as a function of diameter of the nanopore (the graphene nanopores (denoted as GRP) and CNTs have similar diameter). For CNTs, friction decreases with an increase in diameter (except the single-file (6,6) CNT) as small diameters exhibit larger friction at the ends. This is in contrast with the behavior in infinitely long CNTs where a periodic boundary condition is applied with no ends. Viscosity in monolayer graphene is higher for smaller diameters because of stronger density layering along the flow direction. As the diameter increases, viscosity approaches its bulk value in both graphene nanopores and CNTs. Slip length increases for CNTs (except for the single-file (6,6) CNT) and decreases for graphene with an increase in diameter following the scaling of the viscosity-to-friction coefficient ratio. Unlike infinitely long CNTs, slip length increases with diameter for finite-length CNTs especially for shorter CNTs (e.g., 5.34 nm) where the end effects are dominant.

$\lambda$  and  $\mu$  decrease with the increase in the thickness of the pore ( $h$ ) as shown in Figure 2a-b. Significant variation of  $\lambda$  and  $\mu$  is observed as we approach smaller thicknesses, especially for the monolayer graphene case. For long CNTs,  $\lambda$  is dominated by the low friction approaching the limiting friction value of infinitely long CNTs (where a periodic boundary condition is applied along the CNTs in MD simulations).<sup>8</sup> As the membrane becomes thinner (short CNTs and graphene nanopores),  $\lambda$  increases due to the significantly high friction at the ends of the pores (see Figure S6 of the Supporting Information for the variation of friction coefficient along the length of the nanotube).  $\mu$  is higher in graphene nanopores (higher than the bulk value,  $\mu_{\text{bulk}} = 0.85$  mPa s) owing to the highly layered structure of water in the direction of the flow in the nanopore. The axial density variation in a graphene nanopore is shown to be correlated with viscosity.<sup>21</sup> For CNTs, large density

variations only exist at the ends of the tube (see Figure S7 of the Supporting Information for the variation of water density along the length of the CNT). As the thickness increases, the overall  $\mu$  inside the tubes is influenced to a lesser degree by the density fluctuations at the ends (Figure S6 of the Supporting Information shows the variation of viscosity along the length of the nanotube) and is dominated by the lower viscosity observed<sup>25,28</sup> inside the nanotube for an infinitely long CNT. Slip length,  $\delta$ , which is the ratio of viscosity to friction ( $\delta = \frac{\mu}{\lambda}$ ), is directly obtained from NEMD simulations using  $\delta = \frac{\mu U_{\text{slip}}}{\tau_{\text{interface}}}$ , where  $U_{\text{slip}}$  is the slip velocity, and  $\tau_{\text{interface}}$  is the friction force per unit area of the pore. We obtained the slip lengths directly from NEMD to reduce the large error bar associated with the calculation of viscosity and friction coefficients obtained from EMD (both NEMD and EMD simulations result in comparable

slip lengths within the error bars).  $\delta$  increases with the thickness of the pore for most cases (anomalous behavior in small diameter pores is discussed later in this paper) as shown in Figure 2c. Since the variation of  $\lambda$  with the physical thickness of the pore ( $\sim h^{-0.7}$ ) is more significant compared to that of  $\mu$  ( $\sim h^{-0.5}$ ), slip length (which is the ratio of  $\mu$  to  $\lambda$ ) increases with thickness (scaling is based on the range of thicknesses considered here). For longer CNTs (e.g.,  $h = 20.34$  nm), the values of viscosity and friction start to converge to those of infinitely long CNTs. The increasing slip length with thickness is consistent with the velocity profiles observed for graphene nanopores and infinitely long CNTs. In graphene, the radial velocity profile is more parabolic<sup>23</sup> (with a lower  $\delta$ ) compared to the plug-like velocity profiles in CNTs (with a higher  $\delta$ ).<sup>7</sup> The calculated slip lengths in the finite-length CNTs are 1 order of magnitude lower than the values reported in previous simulations<sup>8,25,29</sup> where the slip lengths are calculated for infinitely long CNTs without considering the end effects. We note that the slip lengths (of the order of 70 to 80 nm for very large diameters)<sup>8,29</sup> in simulations for infinitely long CNTs are lower than the slip lengths ( $\sim 300$  nm) observed for long CNTs (with a thickness of  $\sim 1,000$  nm) in experiments.<sup>17</sup> Secchi et al.<sup>17</sup> suggested that the large slip length could be due to the lack of understanding of the electronic structure of interfaces. In addition to force fields, accurate calculation of slip lengths from experimentally measured permeation rates depends on the theory used to describe the flow inside the CNTs as well as the resistance at the ends.

The scaling of  $\lambda$ ,  $\mu$ , and  $\delta$  with the diameter of the pore is shown in Figure 3. For finite-length CNTs,  $\lambda$  reduces (except for the single-file (6,6) CNT) with increasing diameter. This is in contrast to the trend for infinitely long CNTs where the friction coefficient increases with diameter, reaching a maximum value equal to that of the zero-curvature nanochannel<sup>8</sup> ( $\lambda_{\text{flat}} = 1.1 \times 10^4$  N s m<sup>-3</sup>). In infinitely long CNTs, where the effect of the ends is ignored, the friction is mainly governed by the degree of curvature<sup>8</sup> of the CNTs. However, for finite-length CNTs, friction at the ends of the tube's wall dominates, and it increases as the diameter decreases. As the thickness of CNT increases (e.g., 20.34 nm), the end effects become less dominant, and the scaling behavior approaches that of an infinitely long CNT. The (6,6) CNT exhibits a very low friction coefficient. Falk et al.<sup>8</sup> showed that for single-file water in CNTs, the force amplitude or the force in the  $z$  direction between the water and CNT wall almost vanishes (the friction coefficient can be obtained from  $\lambda = \frac{\tau}{K_B T} \rho f^2 S(q)$ , where  $\tau$  is the relaxation time of the force autocorrelation function,  $\rho$  is the surface density of water,  $f$  is the force amplitude (the force per particle from the wall),  $S(q)$  is the structure factor of water, and  $q$  is the wavenumber). To further investigate the low friction coefficient in (6,6) CNTs, we plotted the force autocorrelation function (FACF) for different CNT diameters in Figure S5 of the Supporting Information. The magnitude of FACF at  $t = 0$  ( $\langle F(0)^2 \rangle$ ), is shown to be the smallest for the (6,6) CNT consistent with the explanation of low force amplitude by Falk et al.<sup>8</sup> In addition, the relaxation time of FACF for the (6,6) CNT is small, which leads to a smaller friction coefficient, compared to other CNTs (for more details, see the Supporting Information). For the graphene nanopore case (see Figure 3a),  $\lambda$  exhibits a small increase with the increase in diameter until it reaches the value equal to that of the zero-curvature single-layer graphene slit. In Figure 3b,  $\mu$  is plotted for the graphene nanopores as a function of the pore

diameter, and a value higher than that of the bulk viscosity is observed for the pore diameters considered.  $\mu$  decreases with diameter as the structural layering of water along the axis of the pore ( $z$  direction) starts to vanish for a larger pore diameter. For very small diameter nanopores (subnanometers), inside the pore, the bulk-like region vanishes, and viscosity is dominated by the low interfacial viscosity. In CNTs (Figure 3c),  $\mu$  is lower than the bulk viscosity and increases with the diameter until it reaches the bulk value for large enough tubes (as large diameter CNTs have larger bulk-like region, compared to small diameter CNTs). In small diameter CNTs, the overall effective viscosity is affected by the low viscosity near the surface. Low viscosity near the surface is explained by higher than the bulk diffusion coefficient near the surface<sup>25</sup> (viscosity and diffusion are inversely related by the Einstein relation). Diffusion coefficient increases as the hydrogen bonding is weakened near the surface.<sup>30</sup> Slip length, in finite-length CNTs, increases with diameter as the ratio of viscosity-to-friction coefficient increases with diameter as shown in Figure 3d (viscosity increases with diameter and friction decreases with diameter). Slip length in graphene, however, decreases with diameter as viscosity decreases and friction increases with diameter.

Water viscosity and friction coefficient exhibit length-scale dependence, e.g., variation with thickness of the CNT. The effective viscosity and friction coefficient for a given radius can be obtained from the weighted average of the values in the end regions ( $\mu^e$  and  $\lambda^e$ ) and in the middle section of CNT ( $\mu^\infty$  and  $\lambda^\infty$  (modeled by infinitely long CNTs)). These effective parameters are subsequently used in a simplified single-form HP equation (discussed in the next section of the manuscript) without separately calculating the contribution from the end region and the middle section of CNT. For a given radius ( $r$ ), viscosity and friction coefficient variation with thickness for finite-length CNTs can be expressed as

$$\mu(h, r) = \frac{l \cdot \mu^e(r) + (h - l) \cdot \mu^\infty(r)}{h}$$

and

$$\lambda(h, r) = \frac{l \cdot \lambda^e(r) + (h - l) \cdot \lambda^\infty(r)}{h}$$

where  $l$  denotes the total length of the end regions at both ends of the tube (see Figure 1c). We define  $l$  as a function of  $h$  and  $x_e$  ( $x_e$  is the length of the region at one end, see Figure 1) using  $l = 2x_e(1 - e^{-\frac{h}{2x_e}})$  where  $l$  approaches  $2x_e$  for large  $h$  ( $h > 2x_e$ ) and  $l$  approaches  $h$  for small  $h$  ( $h < 2x_e$ ). As shown in Figure S6, most of the variation of viscosity and friction coefficient takes place within 0.7 nm of the edge of the nanotube (the end region length at one end of the nanotube is set to be  $x_e = 0.7$  nm). The expressions given above are found to describe the thickness variation of viscosity and friction coefficient (see Figure S2 in the Supporting Information). As shown in Figure S6 of the Supporting Information, viscosity and friction vary along the length of the CNT; therefore, viscosity and friction in the end regions ( $\mu^e$  and  $\lambda^e$ ) and in the middle section of the nanopore ( $\mu^\infty$  and  $\lambda^\infty$ ) are different for different radii of the CNT. Variation of viscosity with radius is obtained as a weighted average of viscosities in the interface (denoted by  $\mu_i$  with a layer thickness of  $d_i$  (see Figure 1d)) and in the bulk region of the CNT using  $\mu(r) = \mu_i \frac{A_i(r)}{A_T(r)} + \mu_{\text{bulk}} \left( 1 - \frac{A_i(r)}{A_T(r)} \right)$ , where  $A_i$  and  $A_T$  are the interfacial and total cross-sectional areas of CNTs,

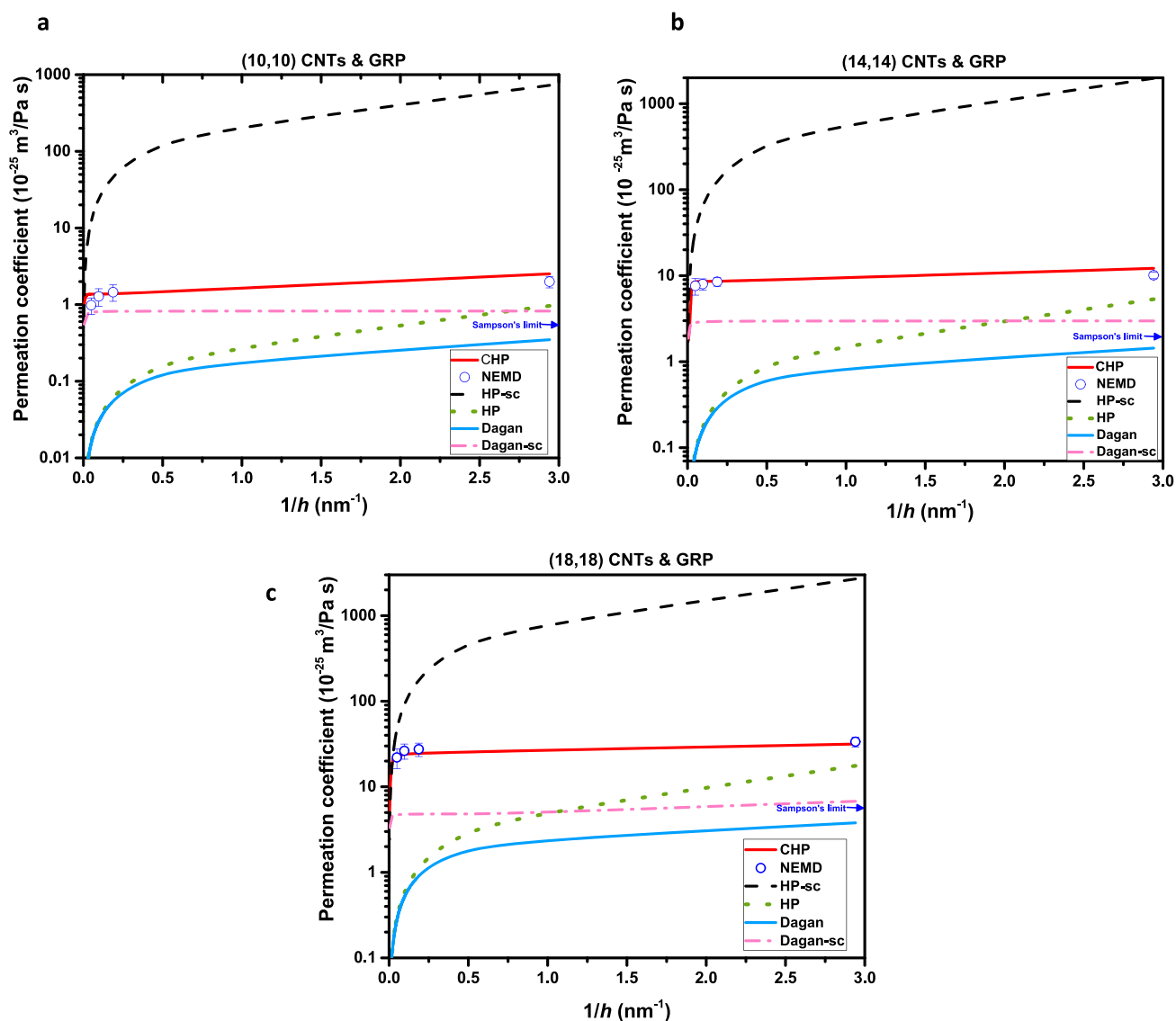


Figure 4. Permeation coefficients of monolayer graphene and finite-length CNTs from pressure driven NEMD simulations (blue circles) are compared with the corrected-HP model ( $P_Q^{\text{CHP}}$ , red solid line) and other theoretical models (HP with viscosity and friction from infinitely long CNTs ( $P_Q^{\text{HP-sc}}$ , black dashed line), no-slip HP with bulk viscosity ( $P_Q^{\text{HP}}$ , green dotted line), Dagan's model ( $P_Q^{\text{Dagan}}$ , blue solid line), and Dagan's model with viscosity and friction from infinitely long CNTs ( $P_Q^{\text{Dagan-sc}}$ , pink dashed and dotted line)) for a. (10,10), b. (14,14), and c. (18,18) CNTs and similar graphene nanopore sizes. The limit of Sampson's model (Dagan's model with  $h \rightarrow 0$ ) is also shown by a blue arrow. The corrected HP theory predicts the permeation from NEMD simulations reasonably well. For long CNTs, no-slip HP and Dagan theories fail as they do not account for the slippage in long CNTs. Slip-HP fails as it overestimates the slippage for short nanopores. Slip-Dagan fails for short nanopores since it overestimates the resistance modeled by the Sampson theory.

respectively.<sup>25</sup> Expressing  $A_i$  and  $A_T$  in terms of  $r$  and  $d_i$ , the variation of  $\mu^e$  and  $\mu^\infty$  with radius is reduced to

$$\mu^e(r) = \frac{(d_i)^2(\mu_{\text{bulk}} - \mu_i^e)}{r^2} - \frac{2d_i(\mu_{\text{bulk}} - \mu_i^e)}{r} + \mu_{\text{bulk}} \quad (\text{Pas})$$

and

$$\mu^\infty(r) = \frac{(d_i)^2(\mu_{\text{bulk}} - \mu_i^\infty)}{r^2} - \frac{2d_i(\mu_{\text{bulk}} - \mu_i^\infty)}{r} + \mu_{\text{bulk}} \quad (\text{Pas})$$

where  $\mu_i^e$ ,  $\mu_i^\infty$ , and  $d_i$  are  $9.5 \times 10^{-4} \text{ Pa s}$ ,  $3.2 \times 10^{-4} \text{ Pa s}$ , and  $0.38 \text{ nm}$ , respectively. See the Supporting Information (Figures S3

and S4) for details on the variation of viscosity with radius. The variation of  $\lambda^e$  and  $\lambda^\infty$  with radius are expressed using the power law form as

$$\lambda^e(r) = C_1 r^{\alpha_1} + \lambda_{\text{slit}} \quad (\text{N s m}^{-3})$$

and

$$\lambda^\infty(r) = C_2 r^{\alpha_2} + \lambda_{\text{flat}} \quad (\text{N s m}^{-3})$$

where the coefficients  $C_1$  and  $C_2$  and exponents  $\alpha_1$  and  $\alpha_2$  are  $5.9 \times 10^4 \text{ N s m}^{-3} \text{ nm}^{3.5}$ ,  $-6.3 \times 10^3 \text{ N s m}^{-3} \text{ nm}^{0.6}$ ,  $-3.5$ , and  $-0.6$ , respectively.  $\lambda_{\text{slit}} = 4.2 \times 10^5 \text{ N s m}^{-3}$  and  $\lambda_{\text{flat}} = 1.1 \times 10^4 \text{ N s m}^{-3}$  are the friction coefficient in a slit with a thickness of  $x_e$  and a nanochannel with two flat parallel graphene sheets, respectively ( $r \rightarrow \infty$ ).  $r$  (accessible radius of CNTs) and  $h$  are in nm. See the

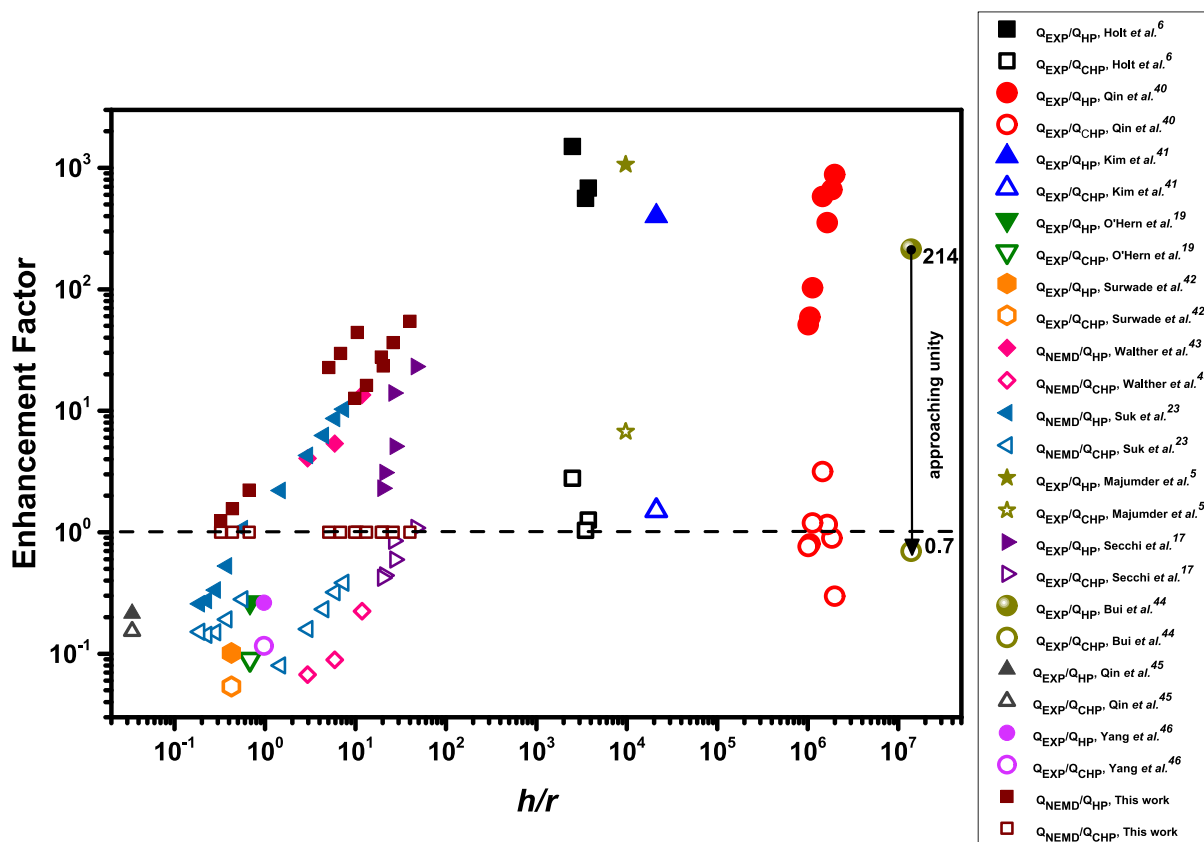


Figure 5. Enhancement factors using the classical no-slip HP theory (filled symbols) and the corrected-HP theory (hollow symbols) are shown for different pore sizes as a function of the physical thickness-to-radius ratio for various experimental and computational permeation coefficients.<sup>5,6,17,19,23,40–46</sup> The previously reported enhancement factors based on the classical HP theory (of the order of 1000 for long CNTs) approach unity when the permeations are normalized by that of the corrected-HP theory. We show this for one of the experimental measurements (Bui et al.<sup>44</sup>) by an arrow ( $\frac{Q_{\text{EXP}}}{Q_{\text{HP}}} = 214 \rightarrow \frac{Q_{\text{EXP}}}{Q_{\text{CHP}}} = 0.7$ ).

Supporting Information (Figure S4) for more details on the variation of friction coefficient with radius.

**Pressure Driven Flows.** Permeation coefficient ( $P_Q = \frac{Q}{\Delta P}$ ), defined as the volumetric flow rate ( $Q$ ) normalized by the applied pressure difference across the pore ( $\Delta P$ ), is obtained from the HP equation. The permeation coefficient determined from the HP equation with a slip condition,  $P_Q^{\text{CHP}} = \frac{\pi(r^4 + 4r^3 \frac{\mu(h,r)}{\lambda_{\infty}})}{8\mu(h,r)} \frac{1}{h_1^{\text{Dagan}}}$ , is corrected by taking into account the variation of  $\lambda$ ,  $\mu$ , and  $\delta$  with thickness and diameter of the nanopore. In addition, the thickness in the corrected-HP (CHP) is the distance over which the pressure drops. Dagan et al.<sup>31</sup> developed a theory for pressure driven Stokes flow through an orifice in which the effective hydrodynamic pressure drop length is estimated to be a function of radius and thickness of the orifice as  $h_1^{\text{Dagan}} = h + \frac{3}{8}\pi r$ . The permeation coefficient predicted by the CHP is shown in Figure 4 as a function of the reciprocal thickness of the pore for three different diameters corresponding to CNTs of (10, 10), (14, 14), and (18, 18). We note that the CHP theory is able to reasonably match the water permeation coefficient from NEMD simulations (used as the reference method) for all the thickness and diameter variations considered in this study. In NEMD, different pressure drops, ranging from 10 to 50 MPa, are applied to obtain the reference permeation coefficients presented as blue circles in Figure 4. For subnanometer pores (e.g., single-file water flow in (6,6))

where the water flow is anomalous and is governed by a hopping mechanism,<sup>23</sup> the CHP fails to predict the permeation coefficients from NEMD simulations. We also plotted the permeation coefficients obtained from other models in Figure 4. The HP equation with a slip condition, where viscosity and friction coefficient are taken from an infinitely long CNT ( $P_Q^{\text{HP-sc}} = \frac{\pi(r^4 + 4r^3 \frac{\mu_{\infty}}{\lambda_{\infty}})}{8\mu_{\infty}} \frac{1}{h}$ ), fails to predict  $P_Q$  for the graphene nanopores and short CNTs as it overestimates the slip length ( $\frac{\mu_{\infty}}{\lambda_{\infty}}$ ) for thin membranes. As shown in Figure 2, slip length decreases as the thickness of the membrane decreases. The HP equation with no-slip condition and bulk viscosity ( $P_Q^{\text{HP}} = \frac{\pi r^4}{8\mu_{\text{bulk}}} \frac{1}{h}$ ) fails for the thicknesses considered, and the deviation grows for longer tubes where the slippage becomes more dominant. The permeation coefficient estimated by Dagan's equation,  $P_Q^{\text{Dagan}} = \frac{\pi r^4}{8\mu_{\text{bulk}}} \frac{1}{(h + \frac{3}{8}\pi r)}$ , fails to match the NEMD results (see Figure 4) mainly due to the lack of slippage in the model. For infinitesimally thin membranes ( $h \rightarrow 0$ ), Dagan's solution reduces to Sampson's equation which serves as the upper limit for the no-slip Stokes flow permeation coefficient through an orifice. We should note that Dagan's equation is simply the HP with no-slip condition with a correction to the hydrodynamic pressure drop length. Using MD simulations, Suk

et al.<sup>21</sup> introduced an empirical relationship for the hydrodynamic pressure drop length,  $h_i^{\text{GRA}} = 0.27r + 0.95$  nm in a monolayer graphene pore. As shown in Figure S8, Dagan's and HP with no-slip condition result in identical permeation coefficients when Suk's empirical relationship is used for the thickness in HP with no-slip condition. We also introduced the

$$\text{slip term in Dagan's equation} \left( P_Q^{\text{Dagan-sc}} = \frac{\pi(r^4 + 4r^3 \frac{\mu_\infty}{\lambda_\infty})}{8\mu_\infty(h + \frac{3}{8}\pi r + \frac{3}{2}\pi \frac{\mu_\infty}{\lambda_\infty})} \right)$$

using the viscosity and friction coefficient from that of an infinitely long CNT. Dagan's equation with a constant slip condition also fails for thin membranes as it overestimates the resistance modeled by Sampson (this is evident as the permeations by Sampson are lower than the permeations in a monolayer graphene nanopore from NEMD). In general, accurate variations of viscosity, friction, and slip length with thickness and diameter as well as a proper hydrodynamic pressure drop length are required for a complete model. The individual contribution for the corrections of viscosity, friction, and hydrodynamic pressure drop length is discussed in the Supporting Information (see Figure S9).

**Enhancement Factors.** In experiments, water transport rates in CNTs have been shown to be enhanced by several orders of magnitude over the rates predicted by the no-slip HP theory. Holt et al.<sup>6</sup> attributed this enhancement to the large slippage at the frictionless CNT surface, and enhancement factors of 100–1000 over no-slip HP flow rates were reported. The validity of the HP equation for small diameter CNTs was questioned<sup>25,32</sup> because of the giant slip lengths<sup>5,6,17</sup> and the lack of understanding of the scaling of hydrodynamic properties with CNT sizes. With the HP equation corrected to account for the variation of viscosity and slip length with the diameter of CNTs, the enhancement factor was reassessed<sup>21,24</sup> as  $\frac{Q_{\text{slip}}}{Q_{\text{no-slip}}} = \left(1 + \frac{4\delta(r)}{r}\right) \frac{\mu_{\text{bulk}}}{\mu(r)}$ . Suk et al.<sup>29</sup> included the effect of finite-length CNTs by modeling the entrance friction using Sampson's equation and reassessed the enhancement factor based on the thickness and diameter of CNTs; here, a direct investigation of the variation of hydrodynamic properties with both diameter and thickness of the pores, including single-layer graphene nanopores, was performed. Figure 5 shows the enhancement factors reported in the literature for various nanopores and CNTs. The data includes both experiments and computations as well as some NEMD calculations performed in this study. When the enhancement factors (from experiments and NEMD simulations) were reassessed using the corrected HP theory, they approach unity. As shown in Figure 5 for most thickness-to-radius ratios ( $\frac{h}{r}$ ), the permeations obtained from the CHP theory approach unity and are in reasonable agreement with experiments, especially for larger values of  $\frac{h}{r}$ . For graphene, the permeation coefficients are overestimated by the CHP theory, and the enhancement factors are below one. Possible explanations for this discrepancy are (i) the lack of accurate force-fields for graphene nanopores where quantum and other effects could be important and affect the scaling of hydrodynamic parameters, (ii) challenging flow rate measurements and existence of defects and contaminants in experiments,<sup>17,19</sup> (iii) inaccurate prediction (by Dagan) of the actual hydrodynamic pressure drop distance, *etc.* For some of the long CNTs, the permeation coefficients are underestimated by the CHP (leading to enhancement factors higher than 1) which one might

find counterintuitive due to the presence of defects and contaminants in experiments. However, the presence of defects and contaminants in experiments can also result in flow enhancement in some cases. It was shown that pure graphene (in vacuum conditions) is more hydrophilic (the force fields used in this work) than the graphene contaminated in air.<sup>33</sup> Enhanced hydrophobicity (especially in the case of long CNTs) results in faster water flow rates in experiments. In addition, it was shown that hydroxyl groups at the edge of nanopores can enhance the flow rates by attracting water molecules toward the nanopore.<sup>10</sup> Therefore, enhancement factors of both higher and lower than 1 should be expected. There is also some discrepancy between the permeations predicted by CHP and other NEMD studies. This is mainly due to the use of different force-fields. In our study, we used the force-field developed by Wu et al.<sup>34</sup> which reasonably matches the experimental water contact angle on graphene.

## CONCLUSION

Flow rates in carbon-based nanopores far exceed the predicted HP flow rates; therefore, in the absence of a theory that accounts for the microscopic physics of transport in nanopores, large enhancement factors were reported. When the microscopic physics is incorporated into the HP theory, the previously reported enhancement factors (of the order of 1000) approach unity. To develop the corrected HP model, the variation of hydrodynamical properties (friction coefficient, viscosity, and slip length) with the thickness and diameter are calculated using Green–Kubo relations and molecular dynamics simulations. Significant variations are observed as the thickness approaches the infinitesimal thickness of the single-layer graphene nanopore. Flow in long CNTs is enhanced by the smooth and frictionless nature of the tube surface where a high slippage occurs. As the thickness reduces, flow rates are dominated by high interfacial friction and viscosity at the pore end regions. For friction coefficient and viscosity, size dependent relations are introduced. Permeation coefficients from the corrected Hagen–Poiseuille model, based on the friction and viscosity relations, successfully predict the values from experiments and molecular dynamics simulations.

## METHODS

MD simulations were performed using the LAMMPS package.<sup>35</sup> The SPC/E water model was used, and the SHAKE algorithm was employed to maintain the rigidity of the water molecule. The carbon–water interactions were modeled by the force-field parameters given in Wu et al.<sup>34</sup> Since the carbon atoms are fixed in space, the interactions between carbon atoms were turned off. We should note that fixing the carbon atoms can lead to flow rate errors of 10%–20% due to lower friction.<sup>7,36</sup> Since flexible membranes add complexity to the calculation of different properties in the radial direction, the effect of flexibility is neglected in this study. The LJ cutoff distance was 12 Å. The long-range electrostatic interactions were calculated by the Particle–Particle–Mesh (PPPM) method.<sup>37</sup> Periodic boundary conditions were applied in all three directions. For each simulation, first the energy of the system was minimized for 10000 steps. Next, the system was equilibrated using the NPT ensemble for 1 ns at a pressure of 1 atm and a temperature of 300 K with a time-step of 1 fs. With the graphene atoms held fixed in space, the NPT simulations allow the water to reach its equilibrium density (1 g/cm<sup>3</sup>). Then, an additional NVT simulation was performed for 2 ns to further equilibrate the system. Temperature was maintained at 300 K by using the Nosé–Hoover thermostat with a time constant of 0.1 ps.<sup>38,39</sup> Finally, the production equilibrium and nonequilibrium simulations were carried out in the NVT ensemble for 20 ns.

## ASSOCIATED CONTENT

## Supporting Information

The Supporting Information is available free of charge at <https://pubs.acs.org/doi/10.1021/acsnano.9b04328>.

Additional details of Green–Kubo auto correlation functions (Figure S1), variation of viscosity and friction with thickness and radius (Figures S2–S6), variation of water density along length of CNTs (Figure S7), Dagan and HP theories with empirically corrected pressure drop length (Figure S8), and contribution of correction of viscosity, friction, and hydrodynamic pressure drop length to CHP model (Figure S9) (PDF)

## AUTHOR INFORMATION

## Corresponding Author

\*E-mail: [aluru@illinois.edu](mailto:aluru@illinois.edu).

## ORCID

Mohammad Heiranian: 0000-0002-2227-4948

## Notes

The authors declare no competing financial interest.

## ACKNOWLEDGMENTS

This work was supported as part of the Center for Enhanced Nanofluidic Transport (CENT), an Energy Frontier Research Center funded by the U.S. Department of Energy, Office of Science, Basic Energy Sciences under Award # DE-SC0019112. The simulations were performed using the Extreme Science and Engineering Discovery Environment (XSEDE) (supported by National Science Foundation (NSF) Grant No. OCI1053575) and Blue Waters (supported by NSF awards OCI-0725070, ACI-1238993 and the state of Illinois).

## REFERENCES

- (1) Liu, K.; Feng, J. D.; Kis, A.; Radenovic, A. Atomically Thin Molybdenum Disulfide Nanopores with High Sensitivity for DNA Translocation. *ACS Nano* **2014**, *8*, 2504–2511.
- (2) Fornasiero, F.; Park, H. G.; Holt, J. K.; Stadermann, M.; Grigoropoulos, C. P.; Noy, A.; Bakajin, O. Ion Exclusion by Sub-2-nm Carbon Nanotube Pores. *Proc. Natl. Acad. Sci. U. S. A.* **2008**, *105*, 17250–17255.
- (3) Koga, K.; Gao, G. T.; Tanaka, H.; Zeng, X. C. Formation of Ordered Ice Nanotubes inside Carbon Nanotubes. *Nature* **2001**, *412*, 802–805.
- (4) Mashl, R. J.; Joseph, S.; Aluru, N. R.; Jakobsson, E. Anomalous Immobilized Water: A New Water Phase Induced by Confinement in Nanotubes. *Nano Lett.* **2003**, *3*, 589–592.
- (5) Majumder, M.; Chopra, N.; Andrews, R.; Hinds, B. J. Nanoscale Hydrodynamics - Enhanced Flow in Carbon Nanotubes. *Nature* **2005**, *438*, 44–44.
- (6) Holt, J. K.; Park, H. G.; Wang, Y.; Stadermann, M.; Artyukhin, A. B.; Grigoropoulos, C. P.; Noy, A.; Bakajin, O. Fast Mass Transport through Sub-2-Nanometer Carbon Nanotubes. *Science* **2006**, *312*, 1034–1037.
- (7) Joseph, S.; Aluru, N. R. Why Are Carbon Nanotubes Fast Transporters of Water? *Nano Lett.* **2008**, *8*, 452–458.
- (8) Falk, K.; Sedlmeier, F.; Joly, L.; Netz, R. R.; Bocquet, L. Molecular Origin of Fast Water Transport in Carbon Nanotube Membranes: Superlubricity versus Curvature Dependent Friction. *Nano Lett.* **2010**, *10*, 4067–4073.
- (9) Farimani, A. B.; Heiranian, M.; Aluru, N. R. Nano-Electro-Mechanical Pump: Giant Pumping of Water in Carbon Nanotubes. *Sci. Rep.* **2016**, *6*, 26211.
- (10) Cohen-Tanugi, D.; Grossman, J. C. Water Desalination across Nanoporous Graphene. *Nano Lett.* **2012**, *12*, 3602–3608.

(11) Heiranian, M.; Farimani, A. B.; Aluru, N. R. Water Desalination with a Single-Layer MoS<sub>2</sub> Nanopore. *Nat. Commun.* **2015**, *6*, 8616.

(12) Feng, J.; Graf, M.; Liu, K.; Ovchinnikov, D.; Dumcenco, D.; Heiranian, M.; Nandigana, V.; Aluru, N. R.; Kis, A.; Radenovic, A. Single-Layer MoS<sub>2</sub> Nanopores as Nanopower Generators. *Nature* **2016**, *536*, 197.

(13) Farimani, A. B.; Min, K.; Aluru, N. R. DNA Base Detection Using a Single-Layer MoS<sub>2</sub>. *ACS Nano* **2014**, *8*, 7914–7922.

(14) Feng, J.; Liu, K.; Bulushev, R. D.; Khlybov, S.; Dumcenco, D.; Kis, A.; Radenovic, A. Identification of Single Nucleotides in MoS<sub>2</sub> Nanopores. *Nat. Nanotechnol.* **2015**, *10*, 1070.

(15) Barati Farimani, A.; Heiranian, M.; Min, K.; Aluru, N. R. Antibody Subclass Detection Using Graphene Nanopores. *J. Phys. Chem. Lett.* **2017**, *8*, 1670–1676.

(16) Hummer, G.; Rasaiah, J. C.; Noworyta, J. P. Water Conduction through the Hydrophobic Channel of a Carbon Nanotube. *Nature* **2001**, *414*, 188–190.

(17) Secchi, E.; Marbach, S.; Niguès, A.; Stein, D.; Siria, A.; Bocquet, L. Massive Radius-Dependent Flow Slippage in Carbon Nanotubes. *Nature* **2016**, *537*, 210–213.

(18) Celebi, K.; Buchheim, J.; Wyss, R. M.; Droudian, A.; Gasser, P.; Shorubalko, I.; Kye, J. I.; Lee, C.; Park, H. G. Ultimate Permeation across Atomically Thin Porous Graphene. *Science* **2014**, *344*, 289–292.

(19) O'Hern, S. C.; Stewart, C. A.; Boutilier, M. S.; Idrobo, J. C.; Bhaviripudi, S.; Das, S. K.; Kong, J.; Laoui, T.; Atieh, M.; Karnik, R. Selective Molecular Transport through Intrinsic Defects in a Single Layer of CVD Graphene. *ACS Nano* **2012**, *6*, 10130–10138.

(20) Xie, Q.; Alibakhshi, M. A.; Jiao, S.; Xu, Z.; Hempel, M.; Kong, J.; Park, H. G.; Duan, C. Fast Water Transport in Graphene Nanofluidic Channels. *Nat. Nanotechnol.* **2018**, *13*, 238.

(21) Suk, M. E.; Aluru, N. R. Molecular and Continuum Hydrodynamics in Graphene Nanopores. *RSC Adv.* **2013**, *3*, 9365–9372.

(22) Buchheim, J.; Schlichting, K. P.; Wyss, R. M.; Park, H. G. Assessing the Thickness-Permeation Paradigm in Nanoporous Membranes. *ACS Nano* **2019**, *13*, 134–142.

(23) Suk, M. E.; Aluru, N. R. Water Transport through Ultrathin Graphene. *J. Phys. Chem. Lett.* **2010**, *1*, 1590–1594.

(24) Thomas, J. A.; McGaughey, A. J. H. Water Flow in Carbon Nanotubes: Transition to Subcontinuum Transport. *Phys. Rev. Lett.* **2009**, *102*, 184502.

(25) Thomas, J. A.; McGaughey, A. J. H. Reassessing Fast Water Transport through Carbon Nanotubes. *Nano Lett.* **2008**, *8*, 2788–2793.

(26) Bocquet, L.; Barrat, J. L. Hydrodynamic Boundary-Conditions, Correlation-Functions, and Kubo Relations for Confined Fluids. *Phys. Rev. E: Stat. Phys., Plasmas, Fluids, Relat. Interdiscip. Top.* **1994**, *49*, 3079–3092.

(27) Zwanzig, R. Time-Correlation Functions and Transport Coefficients in Statistical Mechanics. *Annu. Rev. Phys. Chem.* **1965**, *16*, 67.

(28) Babu, J. S.; Sathian, S. P. The Role of Activation Energy and Reduced Viscosity on the Enhancement of Water Flow through Carbon Nanotubes. *J. Chem. Phys.* **2011**, *134*, 194509.

(29) Suk, M. E.; Aluru, N. R. Modeling Water Flow through Carbon Nanotube Membranes with Entrance/Exit Effects. *Nanoscale Microscale Thermophys. Eng.* **2017**, *21*, 247–262.

(30) Farimani, A. B.; Aluru, N. R. Spatial Diffusion of Water in Carbon Nanotubes: From Fickian to Ballistic Motion. *J. Phys. Chem. B* **2011**, *115*, 12145–12149.

(31) Dagan, Z.; Weinbaum, S.; Pfeffer, R. An Infinite-Series Solution for the Creeping Motion through an Orifice of Finite Length. *J. Fluid Mech.* **1982**, *115*, 505–523.

(32) Verweij, H.; Schillo, M. C.; Li, J. Fast Mass Transport through Carbon Nanotube Membranes. *Small* **2007**, *3*, 1996–2004.

(33) Schrader, M. E. Ultrahigh-Vacuum Techniques in The Measurement of Contact Angles 0.5. LEED Study of the Effect of Structure on the Wettability of Graphite. *J. Phys. Chem.* **1980**, *84*, 2774–2779.

(34) Wu, Y. B.; Aluru, N. R. Graphitic Carbon-Water Nonbonded Interaction Parameters. *J. Phys. Chem. B* **2013**, *117*, 8802–8813.

- (35) Plimpton, S. Fast Parallel Algorithms for Short-Range Molecular-Dynamics. *J. Comput. Phys.* **1995**, *117*, 1–19.
- (36) Sam, A.; Kannam, S. K.; Hartkamp, R.; Sathian, S. P. Water Flow in Carbon Nanotubes: The Effect of Tube Flexibility and Thermostat. *J. Chem. Phys.* **2017**, *146*, 234701.
- (37) Darden, T.; York, D.; Pedersen, L. Particle Mesh Ewald - An NLog(N) Method for Ewald Sums in Large Systems. *J. Chem. Phys.* **1993**, *98*, 10089–10092.
- (38) Nose, S. A Unified Formulation of the Constant Temperature Molecular-Dynamics Methods. *J. Chem. Phys.* **1984**, *81*, 511–519.
- (39) Hoover, W. G. Canonical Dynamics - Equilibrium Phase-Space Distributions. *Phys. Rev. A: At, Mol., Opt. Phys.* **1985**, *31*, 1695–1697.
- (40) Qin, X. C.; Yuan, Q. Z.; Zhao, Y. P.; Xie, S. B.; Liu, Z. F. Measurement of the Rate of Water Translocation through Carbon Nanotubes. *Nano Lett.* **2011**, *11*, 2173–2177.
- (41) Kim, S.; Fornasiero, F.; Park, H. G.; In, J. B.; Meshot, E.; Giraldo, G.; Stadermann, M.; Fireman, M.; Shan, J.; Grigoropoulos, C. P.; Bakajin, O. Fabrication of Flexible, Aligned Carbon Nanotube/Polymer Composite Membranes by *In Situ* Polymerization. *J. Membr. Sci.* **2014**, *460*, 91–98.
- (42) Surwade, S. P.; Smirnov, S. N.; Vlassiuk, I. V.; Unocic, R. R.; Veith, G. M.; Dai, S.; Mahurin, S. M. Water Desalination Using Nanoporous Single-Layer Graphene. *Nat. Nanotechnol.* **2015**, *10*, 459–464.
- (43) Walther, J. H.; Ritos, K.; Cruz-Chu, E. R.; Megaridis, C. M.; Koumoutsakos, P. Barriers to Superfast Water Transport in Carbon Nanotube Membranes. *Nano Lett.* **2013**, *13*, 1910–1914.
- (44) Bui, N.; Meshot, E. R.; Kim, S.; Peña, J.; Gibson, P. W.; Wu, K. J.; Fornasiero, F. Ultrabreathable and Protective Membranes with Sub-5 nm Carbon Nanotube Pores. *Adv. Mater.* **2016**, *28*, 5871.
- (45) Qin, Y.; Hu, Y.; Koehler, S.; Cai, L.; Wen, J.; Tan, X.; Xu, W. L.; Sheng, Q.; Hou, X.; Xue, J.; Yu, M. Ultrafast Nanofiltration through Large-Area Single-Layered Graphene Membranes. *ACS Appl. Mater. Interfaces* **2017**, *9*, 9239–9244.
- (46) Yang, Y.; Yang, X.; Liang, L.; Gao, Y.; Cheng, H.; Li, X.; Zou, M.; Ma, R.; Yuan, Q.; Duan, X. Large-Area Graphene-Nanomesh/Carbon-Nanotube Hybrid Membranes for Ionic and Molecular Nanofiltration. *Science* **2019**, *364*, 1057.